Nanotomographic Observation and Statistical Analysis of Overcharging Induced Cracks in LiCoO₂ Single Crystalline Particles

Andrew Hitt^{1†}, Fan Wang^{1†}, Zeyuan Li¹, Mingyuan Ge², Youtian Zhang¹, Yavuz Savsatli¹, Xianghui Xiao², Wah-Keat Lee², Ryan Stephens³, Ming Tang^{1*}

- Department of Materials Science & NanoEngineering, Rice University, Houston, TX 77005, USA
- National Synchrotron Light Source II, Brookhaven National Laboratory, Upton, NY 11973, USA
- 3. Shell International Exploration and Production Inc., Houston, TX 77082, USA

[†] These authors contributed equally.

^{*}Corresponding author email: mingtang@rice.edu

Abstract

Particle fracture represents an important mode of battery electrode degradation. Extensive cracking occurs in the layered oxide cathodes of lithium-ion rechargeable batteries when they are charged beyond safe operational voltages. In this paper, we analyze the morphology and distribution of cracks in over 100 overcharged LiCoO₂ (LCO) single-crystalline particles imaged via X-ray nanotomography. We observe a strong particle size dependence in both nucleation and growth of cracks, with percentage of cracked particles, crack size, and crack surface area per unit volume all increasing significantly with particle volume. Increasing the cutoff voltage above 4.6V is found to trigger much more pronounced crack growth, which we attribute to the large misfit stress caused by the H1-3 to O1 phase transition. This study offers valuable statistical insights into the fracture behavior of layered oxide cathodes and reveals the importance of particle size control on electromechanical degradation of battery electrodes.

Keywords: Lithium-ion batteries; LiCoO₂ cathode; Overcharging; Cracking; X-ray imaging; Battery degradation

1. Introduction

Mechanical degradation caused by cycling-induced stress is a common and important failure mechanism for electrodes in lithium-ion rechargeable battery (LIBs)¹. Layered lithium transition metal oxides (LiMO₂, M=Ni, Co, Mn), including LiCoO₂ (LCO), LiNi_xCo_yMn_{1-x-y}O₂ (NMC) and LiNi_xCo_yAl_{1-x-y}O₂ (NCA), are among the most common LIB cathode materials, with applications ranging from consumer electronics to electric vehicles. This class of materials is plagued by intergranular fracture (i.e. cracking along weak grain boundaries) in secondary particles during battery operation ²⁻⁴. This intergranular fracture disrupts electronic and ionic transport pathways and increases exposure of the electrode surface to the electrolyte, promoting a host of surface-related degradation mechanisms such as irreversible phase transformations ^{5,6}, electrolyte decomposition ⁷, metal dissolution ^{8,9}, oxygen release ^{10,11} and passivation layer formation ^{12,13}, which cause impedance increase and capacity fade of batteries.

Recently, replacing polycrystalline NMC with single-crystal NMC has led to significant increases in the cycling stability via the elimination of intergranular fracture ^{14,15}. Single-crystalline NMC532 remained virtually crack-free after 5000 cycles, earning it consideration as a cathode for a "million-mile battery" ¹⁴. Similarly, the use of single-crystal NMC622 in NMC/graphite cells demonstrated a 60% increase in cycle life (defined by 80% capacity retention) over its polycrystalline counterpart ¹⁵.

While the use of single-crystal LiMO₂ particles can substantially reduce the effects of intergranular fracture, intragranular fracture can still occur in them especially when cycled above some critical voltage ¹⁵⁻¹⁹. Intragranular fracture is often coupled with other processes that aggravate degradation; in NMC, oxygen release, assisted by facile transport along cracks, causes the preferential formation of the spinel/rock salt structures on crack surfaces ^{16,19}, and in LCO

misfit stress of phase transformations triggers crack propagation at phase boundaries ¹⁸. This yields a maximum delithiation of about 50%, meaning that only half of the available lithium participates in the charging/discharging process. As increasing the upper voltage limit of battery operation is an area of tremendous interest due to its direct relation with reversible energy density of LIB cathodes ^{7,20,21}, understanding high voltage LiMO₂ behavior, including intragranular fracture and its interplay with other degradation mechanisms, becomes especially important.

Both overcharging- and heating-induced intragranular cracks in LiMO₂ have been characterized by electron microscopy (EM) ^{10,15-19,22,23}. These studies reveal that intragranular cracking occurs mainly along the (003) lattice plane, and that cracks can nucleate at internal defect sites, such as dislocations ¹⁶, Ni-Li antisites ¹⁹, and twin boundaries ¹⁸. These findings are in opposition to the commonly assumed surface nucleation of cracks and, more significantly, suggest that fracture does not necessarily expose fresh electrode surface to the electrolyte. Several works also identify a strong coupling between fracture and the instability of the layered structure of LiMO₂ at high voltages, as evidenced by the proximity between the cracks and new phases resulting from the oxide decomposition or phase transitions ¹⁷⁻¹⁹. While these studies provide valuable insight, they are limited in that they only characterize a relatively small number of cracks in two dimensions (2D), which does not allow for a comprehensive statistical analysis of fracture behavior, such as the distribution of cracks within individual particles or within multi-particle ensembles. This leaves outstanding questions requiring the large-scale characterization of intragranular cracks, including but not limited to: (1) how do charging conditions affect the frequency of intragranular fracture, (2) how does particle size affect the occurrence of intragranular fracture, and (3) is crack formation dominated by surface or internal nucleation?

In this work, we employed X-ray nanotomography, based on full-field transmission X-ray microscopy (FF-TXM), to investigate the morphology and distribution of 282 individual cracks in 164 overcharged LCO particles. The large field of view of FF-TXM facilitates the facile characterization of multiple particles and the high spatial resolution allows fine cracks to be resolved. We developed a semi-automatic image processing procedure to efficiently detect and segment both particles and cracks from nanotomography data. While cracks in battery electrode particles have been imaged with similar techniques ^{3,24-28}, our study provides the largest crack segmentation dataset and the first statistical analysis of multi-particle crack distribution in LiMO₂ cathodes to our best knowledge. We observe that overcharging-induced cracks nucleated at both surface and internal sites, including twin boundaries. Crack nucleation and growth both have strong dependence on particle size, with small particles containing fewer and smaller cracks than larger particles. Increases in charging cutoff voltage also yield higher crack density and increased size; a substantial increase in crack surface area occurs when the cutoff voltage is raised above 4.6V, which could be attributed to the substantial misfit stress generated by the H1-3 to O1 phase transformation. The statistical information obtained from this multi-particle characterization complements detailed EM studies of individual cracks in advancing the mechanistic understanding of overcharging-induced mechanical degradation of layered LiMO₂ cathodes.

2. Results

2.1. Synthesis, characterization and electrochemical measurements of single-crystalline LiCoO₂ We used a molten salt method ²⁹ to synthesize single-crystal LCO particles. The obtained particles are micron-scale plates with hexagonal or truncated triangular shapes (Fig. 1a). This morphology is in good agreement with the computed equilibrium crystal shapes of LiCoO₂ (Fig. 1b) previously

reported by Kramer and Ceder ³⁰ using first-principles calculations. Based on the comparison, the basal surface of the plates is identified to be the (003) plane and the side facets are (012) and (104) planes. The particle size ranges between 4 um and 25 um with a mean value of 10.8 um based on estimates from the scanning electron microscopy (SEM) images.

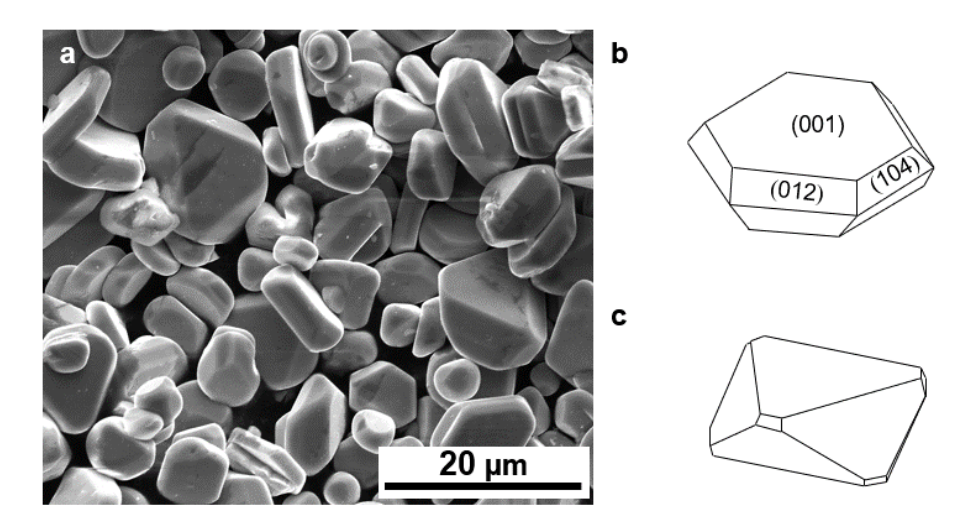


Figure 1 | **LCO** single crystals synthesized by the molten salt method. (a) SEM image of LCO single crystals produced by the molten salt synthesis. (b,c) Equilibrium crystal shapes of LCO in an oxidizing (b) and reducing (c) environment, as determined from first-principles calculations by Kramer and Ceder, the details of which can be found in Ref. 30.

As-synthesized single-crystal LCO particles were charged to 4.8V against Li/Li⁺ at a low rate of 0.05 C (i.e. full charge in 20 hours, 1C = 275 mA/g) and the capacity-voltage data were collected (Fig. 2a). The differential capacity dQ/dV, where Q is capacity and V is voltage, was calculated from the data. Five distinct peaks can be seen on the dQ/dV curve (Fig. 2b), each of which corresponds well to a different phase transition reported in literature: a first-order metal-insulator transition at 3.9V 31 , two order-disorder transitions near Li_{0.5}CoO₂ at 4.1V and 4.2V 32,33 , a transition from the O3 phase to the H1-3 phase at 4.55V, and a transition from the H1-3 phase to the O1 phase at 4.62V 7,34 .

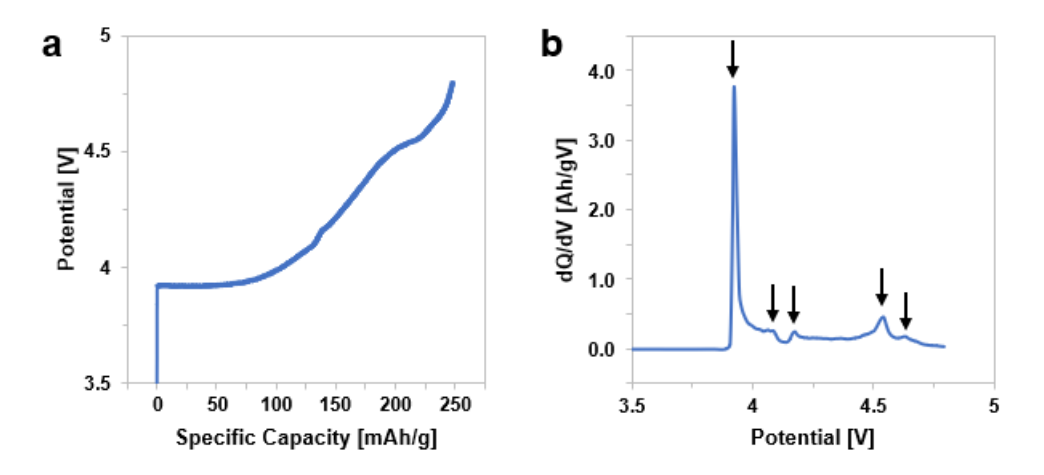


Figure 2 | **Potential and differential capacity curves of LCO half cell. (a)** The potential curve of a fresh LCO half-cell charged to 4.8V at 0.05C (13.75 mA/g). **(b)** The differential capacity curve calculated from the data shown in (a), highlighting the five notable phase transitions peaks.

The latter two transitions (O3 to H1-3 and H1-3 to O1) were believed to be responsible for capacity fade of LCO above 4.5V ³⁵ because of the significant misfit stress generated during the phase transitions. The O3, H1-3 and O1 phases have similar layered structures with different stacking orders of the O-Co-O slabs ³³. O1 can be obtained from O3 by a simple gliding of these slabs in relation to each other. H1-3 is a stage II compound of LixCoO2, with Li intercalating into alternating planes between the O-Co-O slabs, and can be considered a hybrid structure of the O3 and O1 phases with alternating stacking of these phases along the c-axis. To evaluate how these two transitions contribute to LCO fracture, we prepared three LCO electrode samples by charging pristine LCO to 4.5V, 4.6V, and 4.8V for one cycle at a rate of 0.05C. As these three samples experienced none, one, or both phase transitions, respectively, their comparison would demonstrate the effect of each transition.

2.2 Morphology of overcharging-induced cracks

A total of 179 LCO particles were characterized via nanotomography conducted at beamline 18-ID of the National Synchrotron Light Source II (NSLS-II). Among them, 164 particles were from the three overcharged samples and 15 are pristine LCO particles. The lower limit of the crack size that can detected by this method is 40 nm, which is pixel spatial resolution of the reconstructed images. Analyzed particles from the three overcharged samples have similar size distributions (Suppl. Fig. 1). Cracks in the particles were segmented using the analysis procedure described in the Methods section. Particles from the 4.8V sample were individually rendered and viewed orthogonally to the (003) plane, with cracks highlighted in red (Fig. 3). Equivalent visualization was also performed for particles in the 4.5V (Suppl. Fig. 2), 4.6V (Suppl. Fig. 3) and pristine (Suppl. Fig. 4) samples.

As a baseline, we confirmed that the pristine particles are crack-free (Suppl. Fig. 4). With few exceptions, cracks detected in the overcharged samples are parallel to the largest surface facets, which are indexed as (003) planes based on the comparison to the Wulff shape of LCO (Sec. 2.1). This observation is consistent with prior studies of cycling-induced fracture in layered oxide electrodes ¹⁶⁻¹⁸, and confirms that (003) is the dominant cleavage plane due to relatively weak bonding between MO₂ layers. Particles containing multiple parallel (003) cracks were typical in all three samples, with these parallel cracks being visible in both the reconstructed tomography data (Fig. 4a) and the three-dimensional (3D) renders (Fig. 4b).

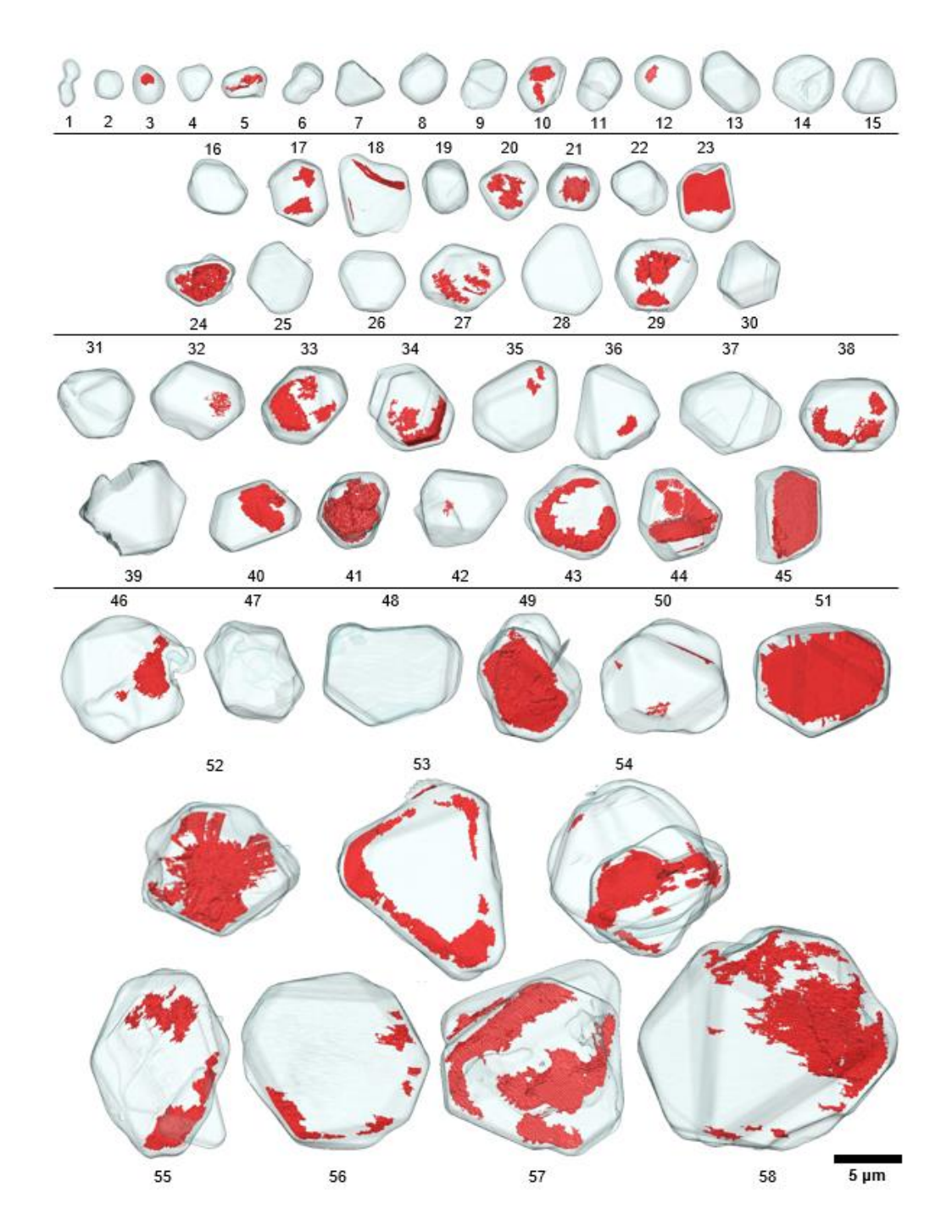


Figure 3 | Renders of LCO particles in the 4.8V sample. Distinct particles from tomographic reconstruction of the LCO sample charged to 4.8 V are individually rendered orthogonal to the (003) plane, with cracks shown in opaque red. Particles are sorted, numbered, and grouped into four size bins (0 to 36 μ m³, 36 to 64 μ m³, 64 to 144 μ m³, 144 μ m³ or larger) by volume for analysis of size dependence.

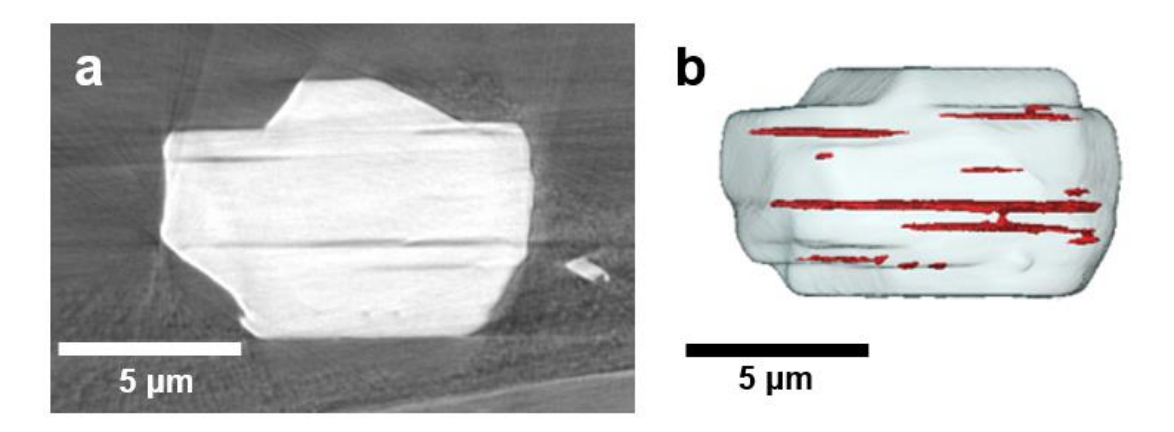


Figure 4 | **A particle showing preferential cracking along parallel (003) planes. (a)** Particle 51 viewed perpendicular to the (003) plane showing parallel cracks along this plane in reconstructed tomogram. (b) 3D rendering of the same particle, with cracks shown in red.

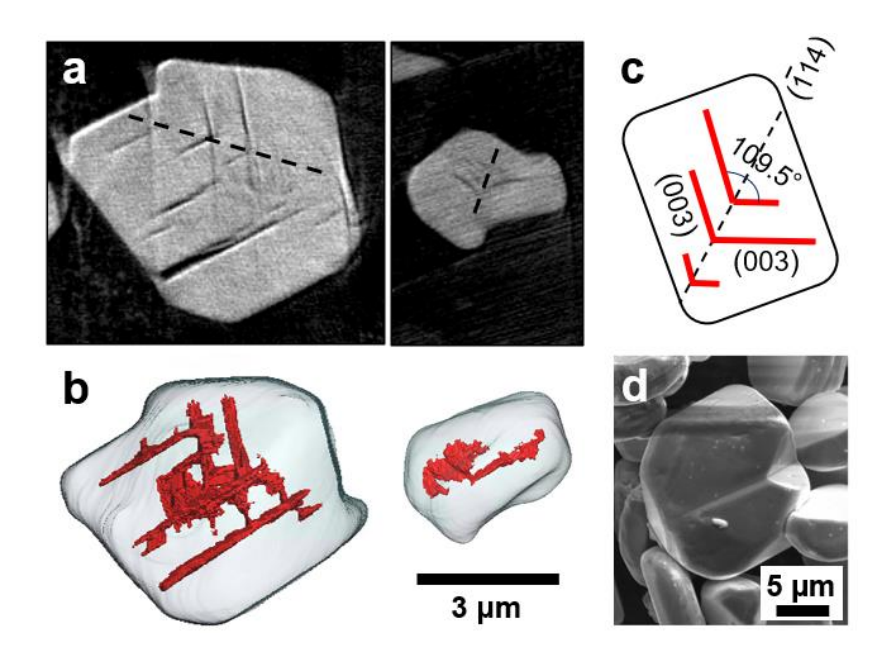


Figure 5 | **Cracking along twin boundaries.** (**a**, **b**) Reconstructed image and 3D rendering of particles 45 and 5 of the 4.8 V sample showing intersecting cracks near a twin boundary. Approximate locations of twin boundaries are shown with dashed lines. (**c**) A schematic of (003) cracks (red) nucleated at ($\overline{1}14$) twin boundary. (**d**) SEM image showing a particle containing twinning crystallites.

As shown in Fig. 5a-b, several particles in the samples were observed to contain two groups of parallel cracks that intersected each other. As it has been established that intragranular cracks in the layered oxide mainly grow in parallel to the (003) planes because of the weak MO_2 layer-layer attraction, these particles are most likely not monocrystalline. This is confirmed by the particle morphology observed in SEM (Fig. 5d), which shows two crystallites fused together and separated by a grain boundary. The angle between the (003) planes in the adjoining crystallites, identified from the orientation of the cracks, was measured to be 109° . This angular relation is in good agreement with a ($\bar{1}14$) twin boundary in LCO (Fig. 5c). Our observation is consistent with a previous transmission electron microscopy study, which found that cracks are prone to nucleating at ($\bar{1}14$) twin boundaries and propagating along (003) planes into grains on both sides in cycled LCO particles 18 .

While the cracks are predominantly parallel to the (003) plane, their locations and shape are more varied. Many cracks exhibit preferential growth along the plate edges (e.g. particle 53 in Fig. 3, particle 65 in Suppl. Fig. 2), which implies that they were nucleated at the particle surface. Some cracks extend across the entire particle (e.g. particle 51 in Fig. 3), and there were also numerous cracks entirely contained within the particles (e.g. particle 21 in Fig. 3). The latter suggests the internal nucleation of cracks. This is corroborated by measuring the crack opening width along the (003) axis, which is visualized in greyscale color scheme for three cracks as shown in Fig. 6a-c. The largest openings of these internal cracks are inside the particles, implying their initiation at internal sites. This agrees with a previous study on the nucleation of cycling-induced intragranular cracks in NMC111 particles ¹⁶, which identified a high density of atomically thin (003) fractures terminating at edge dislocations that are believed to be the precursors of intragranular cracks. Internal nucleation could also be assisted by the presence of Ni-Li antisite defects ¹⁹,

decomposition-induced voids ^{16,18} and buried twin boundaries ¹⁸. Nevertheless, we observe cracks both along the surface and inside the particles, which shows that multiple types of preexisting surface and bulk defects contribute to crack initiation.

We performed SEM analysis of overcharged LCO particles to investigate the surface features that facilitate crack nucleation. As shown in Suppl. Fig. 5a, a common type of planar defects observed in our samples are the (003)-oriented grain boundary between two stacked LCO plates, which share the [003] axis but have different in-plane orientations. Surface grooves developed at locations where the grain boundary intersects the particle surface. Suppl. Fig. 5b illustrates that such surface-notch-like features are weak spots for cracks to nucleate and propagate along the grain boundary. Similar grain boundary cleavage is also visible in tomographic images, see Suppl. Fig. 5d. Nonetheless, the same particles also contain surface-initiated cracks growing inside the LCO crystallites, suggesting that there are other types of contributing surface defects. Bi et al. recently discovered that the lattice of high-Ni NMC single crystals can easily glide along the (003) plane during cycling in response to shear stress generated by non-uniform Li distribution inside the particles ³⁶. We observed similar gliding marks on cycled LCO particles (Suppl. Fig. 5c), which shows that lattice gliding is also common in LCO single crystals during charging and discharging. Gliding micro-steps that formed on the particle surface also provide favorable locations for crack nucleation ³⁶.

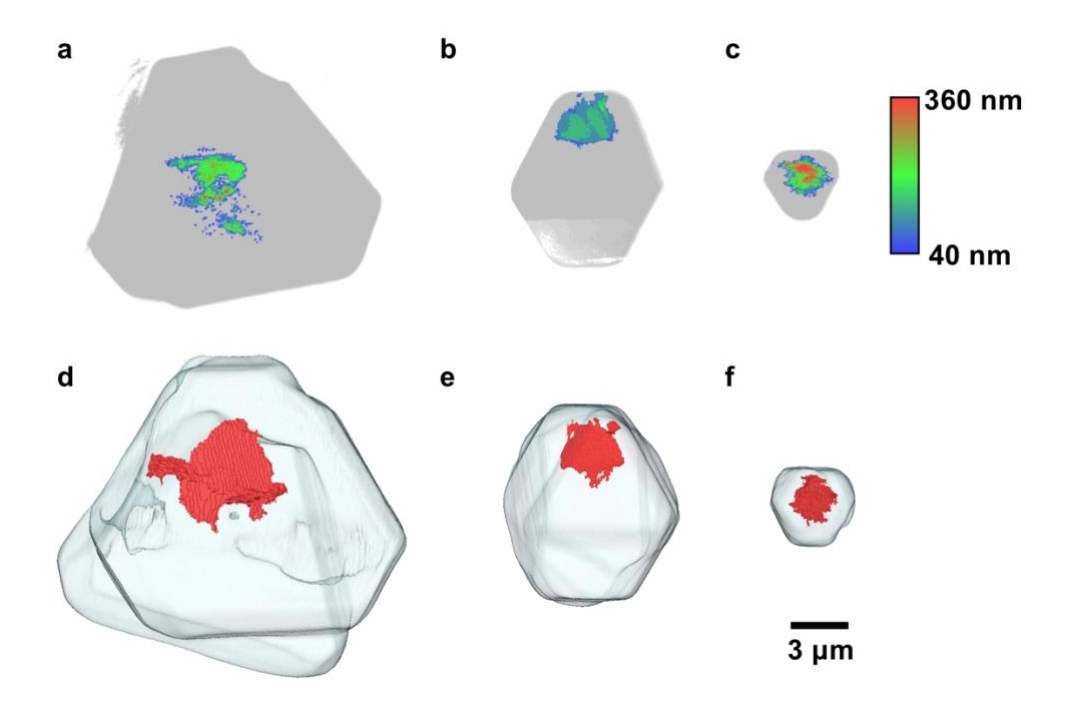


Figure 6 | Internal cracks within LCO particles.

(a-c) Visualization of an internal crack in three particles (from left to right: particle 57, 51 and 21 from the 4.8 V sample). Cracks are shown in pseudo-color coding with the color representing the crack opening width measured from tomographic images. These cracks are the widest inside the particles and become shallower when approaching the particle edges, which suggest they probably nucleated internally. (d-f) 3D renders of the same cracks (shown in red) in the particles.

2.3 Particle size and voltage dependence of crack distribution

We now turn attention to the multi-particle distribution of overcharging-induced fracture. Overall, there were 164 particles analyzed from the three samples, of which 98 contained some degree of cracks (Table 1).

Table 1 | Summary of analyzed overcharged LCO particles

Cutoff Voltage [V]	Particles	Uncracked Particles	Cracked Particles
4.5	69	37	32
4.6	37	18	19
4.8	58	23	35

Not surprisingly, the overall percentage of fractured particles (f_c) increases with the upper cutoff voltage (Φ_0), with f_c = 46.4%, 51.4% and 60.3% for particles charged to Φ_0 = 4.5V, 4.6V, and 4.8V, respectively (Fig. 7a). In general, raising Φ_0 leads to higher frequency of cracking at all particle volumes. In addition to this voltage effect, the existence of cracks also depends strongly on the particle size, with smaller particles being less likely to fracture. To confirm this, we categorize particles into one of four groups based on volume (V_p = 0 to 36, 36 to 64, 64 to 144, >144 um³), with these selected volume ranges containing approximately equal quantities of particles. As shown in Fig. 7b, for LCO charged to 4.5V, less than 16% of particles with V_p < 36 µm³ contain cracks (compared to 27% of similar particles charged to 4.8V), increasing up to 73% for particles with V_p > 144 µm³ (compared to 85% of similar particles charged to 4.8V).

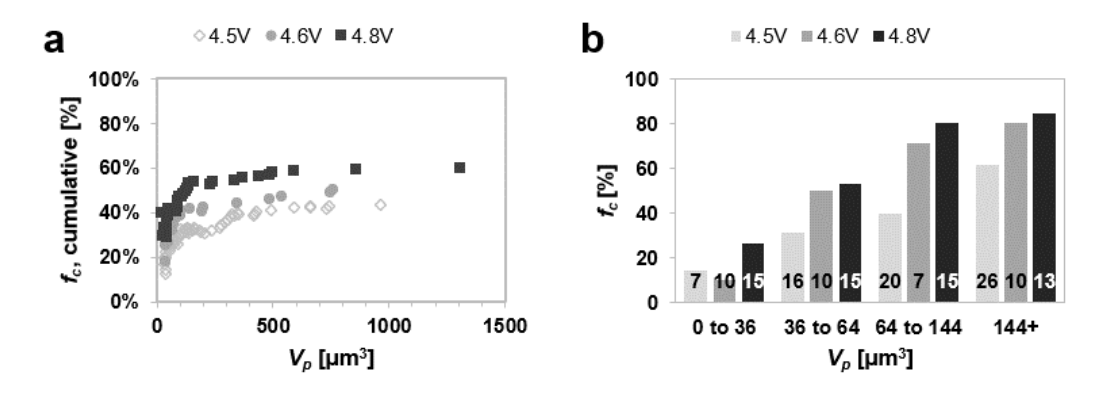


Figure 7 | Effects of particle volume and cycling voltage on crack frequency. (a) The cumulative percentage of crack-containing LCO particles as a function of the upper limit of particle volume V_p . (b) The percentage of LCO particles within a given volume range that contained cracks after charging to a given cycling cutoff voltage (the labels for each bar are the total number of particles in that group).

Particle size and cycling voltage also have an observable effect on crack growth. Calculating the volumetric crack surface area (A_{vol}) for particles grouped by cutoff voltage and volume shows a substantial size effect: the largest particles contained 8.3, 5.5, and 4.1 times the A_{vol} of the smallest particles for LCO charged to 4.5, 4.6, and 4.8V, respectively (Fig. 8a). Examination of the average individual crack size (\bar{A}_c) within particles for a specific cycling voltage and volume range similarly reveals a strong correlation between crack and particle size at all voltages (Fig. 8b). Therefore, larger particles not only have more cracks, but also larger cracks.

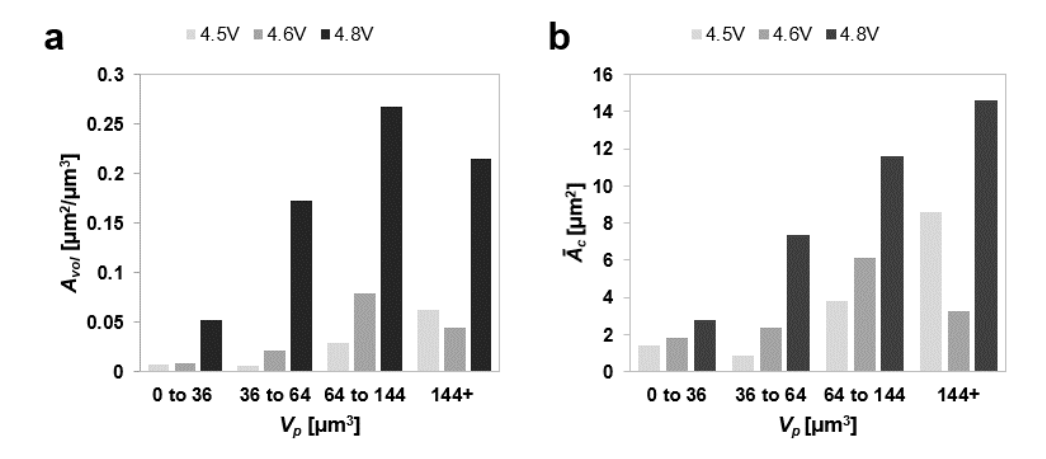


Figure 8 | **Effects of particle volume and cycling voltage on crack growth. (a)** The crack area per unit volume for particles within a given volume range after charging to a given cutoff voltage. **(b)** The average individual crack area for particles within a given volume range after charging to a given cutoff voltage.

We propose that two factors contribute to the observed size dependence of the fracture behavior in LCO particles. The first is that larger particles contain more crack nucleation sites, provided that the density of pre-existing defects for crack initiation does not vary significantly with particle size, and thus they naturally have a higher probability of fracture than smaller ones. As a simple estimate, assume that particles have a uniform defect density (ρ_d) and each pre-

existing defect inside a particle has a probability to form a crack (p), and let $\lambda = -\rho_d \ln p$. The fraction of crack-containing particles varies with particle volume V_P as $f_c = 1 - \exp(-\lambda V_P)$ for crack nucleation dominated by bulk defects, or with surface area A_P as $f_c = 1 - \exp(-\lambda V_P)$ for surface-defect-dominant crack nucleation. We observe that the number of cracks normalized by the surface area of the particle does not vary significantly with particle size (Suppl. Fig. 6a), while the number of cracks normalized by the particle volume shows a notable drop (Suppl. Fig. 6b). This suggests that crack nucleation predominantly occurs at surface defects. Visual inspection of the tomographic images also confirms the dominance of surface cracks (cracks that intersect particle surface) over internally confined cracks although a surface crack may nucleate internally and subsequently reach the surface. As shown in Suppl. Fig. 7, with the exception of particles in the volume range of $0 - 36 \, \mu \text{m}^3$ from the 4.6 V sample, which contain only one crack, internal cracks account for less than 40% of the cracks across particle size bins of all cut-off voltages. We do not observe a strong particle size dependence of the surface to internal crack ratio.

This geometric argument does not explain why smaller particles also have smaller cracks, which must originate from a second particle size effect. Cracks advance during cycling to reduce the elastic energy stored within a particle. The driving force of crack growth is characterized by an energy release rate (G), which quantifies the reduction of the elastic energy in the particle when the crack advances a unit area. When a phase transition occurs in a particle and generates a misfit stress to open the crack, G can be expressed as

$$G = ZE\epsilon_0^2 a \tag{1}$$

where a is the crack feature size, E the elastic modulus of the electrode material, ϵ_0 the misfit strain between the two phases, and E a dimensionless constant that depends on the morphology of the particle and crack. When the particle shape and the crack location within the particle are fixed,

dimensional analysis suggests that Z must be a function of the ratio between the sizes of the particle (L) and the crack (a). Fracture mechanics calculations for a surface crack in a plate-like particle (Suppl. Fig. 8a) with LCO properties shows that Z increases monotonically with L/a and eventually reaches a plateau at large L/a values (Suppl. Fig. 8b). Thus, reducing particle size leads to a decrease in the driving force of the advancement of a crack of a given size, which results in smaller particles containing smaller cracks.

While we assume a specific particle morphology, crack location, and loading condition in the calculation, the observed size dependence is a general result 1,15,37 . Intuitively, this is because small particle sizes enhance the relaxation of internal stress through the free surfaces, thus reducing the strain energy release rate associated with crack growth. Previous works have predicted that insertion-induced cracking in lithium-ion electrode materials could be fully suppressed in particles below a critical size (L_{crit}) 1,37 , which was estimated to be \sim 1 um for NMC622 particles 15 . While the LCO particles analyzed in this work are larger than this critical size, which prevents cracking from being completely averted, we show that reducing particle sizes above the critical size is still beneficial in limiting the extent of fracture in electrode particles.

While both the nucleation (f_c) and growth (A_{vol} , \bar{A}_c) of cracks exhibit strong dependence on particle size, they differ in how they are affected by increases in upper charging cutoff voltage Φ_0 Increasing Φ_0 from 4.6 to 4.8V produces only a modest increase in f_c , which suggests that crack nucleation upon charging is primarily controlled by pre-existing surface or bulk defects (e.g. crack-like surface flaws, edge dislocations, or voids). However, increasing Φ_0 from 4.6 to 4.8V yields significant increases in A_{vol} (factor of 3 to 8) and \bar{A}_c (factor of 1.5 to 4.5) across the four volume categories. Plotting the cumulative crack surface area (A_{tot}) against the cumulative particle volume (V_{tot}) reveals that the 4.8V sample has more than 4 times the crack area of the 4.5 and 4.6V samples

(Fig. 9), despite the three samples having similar size distributions of cracked particles (Suppl. Fig. 1b). In comparison, increasing Φ_0 from 4.5 to 4.6V produces only a slight increase in A_{tot} .

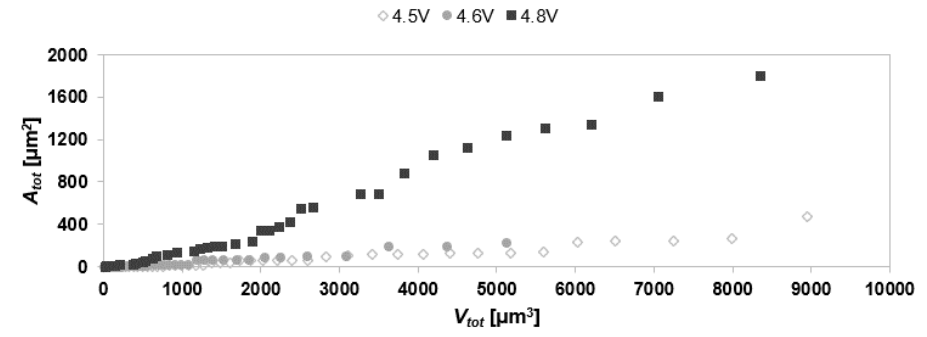


Figure 9 | Comparison of crack surface area across charging cutoff voltages. The cumulative sum of the area of cracks vs the cumulative volume of particles, which are ordered by their volume from small to large values in the plot.

3. Discussion

The results above suggest that the H1-3 to O1 phase transition near 4.62V (Figure 2b) ^{7,35} triggers substantial crack propagation, but that the O3 to H1-3 transition near 4.55V has a much more muted effect. The difference in the effects of these two phase transitions may be attributed to the differences in lattice mismatch, which generates misfit strain energy that facilitates crack growth in LCO particles. At Li_{x≈0.2}CoO₂, the c-lattice misfit between H1-3 and O1 phase is approximately 6% ³⁸, which results in a large tensile stress in the O1 domains, promoting crack formation in the O1 phase and along phase boundaries in LCO cycled above this charging voltage ¹⁸. By comparison, the c-lattice misfit between O3 and H1-3 under the same conditions is only 3%, which could explain why there is no substantial difference in crack growth between particles cycled at 4.5 and 4.6V.

Our study shows that reducing particle size is an effective way to alleviate electrode mechanical degradation caused by cracking. However, overcharging-induced capacity fade involves multiple degradation mechanisms, some of which may also be influenced by particle size.

Delithiation of Lix<0.5CoO2 involves an oxygen redox reaction ³⁹, which destabilizes the host structure and triggers both cobalt dissolution ^{8,9} and oxygen release ¹¹. Electrolyte decomposition at high cycling voltages produces a surface passivation layer on LCO, which causes capacity fade due to impedance growth. As these degradation processes are surface-mediated, their mitigation favors larger particles. These competing size effects imply the existence of an optimal particle size range that maximizes capacity retention. As a simple consideration, assume that the capacity fade is proportional to the total area of the particle surface and cycling-induced crack surface. Let the volumetric crack surface area A_{vol} depend on particle volume as $A_{vol} = a_1 V_p^{\gamma}$ ($\gamma \approx 1 - 1.4$ estimated from the 4.5 V, 4.6 V and 4.8 V samples) and particle surface area be $a_2V_p^{2/3}$, where a_1 and a_2 are proportionality factors. The total surface area per particle volume and hence capacity loss is minimized at $V_p = \left(\frac{a_2}{3\gamma a_1}\right)^{3/(3\gamma+1)}$. This analysis, though oversimplified, points to the possible benefit of particle size control, a hypothesis that needs to be further examined by carefully designed experiments to quantify the relative contributions of different degradation modes to capacity fade. We also point out that the overcharged LCO samples characterized in this study were subject to only one low-rate charge cycle but already contain a significant amount of cracks that are detectable in nanotomography. This indicates that the extent of cracking in LCO particles overcharged at higher rates and after multiple cycles could be substantial. The cycling effects on crack formation and accumulation in single crystalline LCO will comprise a future study.

4. Conclusion

In summary, a statistical analysis of the morphology and distribution of 282 overcharging-induced cracks in 164 LCO particles was performed via the combination of nanotomography and a semi-automated image processing algorithm. The cracks are predominantly parallel to the (003) plane

and initiated at both surface and internal sites. Crack growth and nucleation were both influenced by particle size, with larger particles containing more and larger cracks, which we attribute to the increases in pre-existing defects and energy release rate from crack advancement in larger particles, respectively. A voltage effect on crack size was also observed, with particles charged to 4.8V containing significantly more crack area per unit volume than particles charged to lower voltages. This effect is likely due to the substantial misfit strain caused by the H1-3 to O1 phase transition that occurs when LCO is charged above 4.62V. While reducing particle size demonstrates an effective way to reduce overcharging-induced fracture, future work on the relative effects of various degradation mechanisms will be required to determine an optimal particle size range to minimize overcharging-induced capacity loss.

5. Methods

5.1. Synthesis of single-crystalline LCO particles

Single crystalline LCO particles were synthesized by a molten salt method ²⁹. Reagent-grade LiOH, Co₃O₄ and NaCl (Sigma-Aldrich) with a molar ratio of 6:1:10 were mixed by ball mill (SPEX), then baked in an alumina crucible at 900°C for 10 hours. The heating and cooling rate was controlled at 5°C/min. After cooling to room temperature, the products were washed with deionized water, centrifuged 3 – 5 times to remove the remaining flux, and then annealed at 750°C for 10 hours to improve the crystallinity of LCO particles.

5.2. Measurement of electrochemical performance

A slurry of 80% (weight percentage) LCO particles, 10% carbon black and 10% poly(vinylidene fluoride) was mixed with N-Methyl-2-pyrrolidone, and then cast on an aluminum foil and dried in vacuum oven at 120C for 12 hours. The dried electrode was punched into 12mm disks and

assembled in CR-2032 coin cells with Celgard 2325 separator, lithium metal anode, and 1 M LiPF6 in ethylene carbonate / dimethyl carbonate (EC/DMC, 1:1 volume ratio) as the electrolyte. Fresh LCO half cells were charged from the fully lithiated state to different voltage cutoffs at 0.05C (1C = 275 mA/g). After charging, coin cells were quickly dissembled in an Ar-filled glovebox to retrieve the LCO electrodes, which were washed with dimethyl carbonate several times and dried in the glovebox overnight.

5.3. Characterization of LCO structure

LCO particle morphology and size were observed in an FEI Quanta 400 scanning electron microscope. Nano-tomography was performed on charged LCO electrodes at beamline 18-ID, NSLS-II, Brookhaven National Laboratory. The incident X-ray energy was fixed at 7.8 keV, slightly above the cobalt absorption K-edge at 7.7 keV. Before the experiments, small sample pieces were cut from the charged LCO electrode discs, sealed between two Kapton films and mounted on a sample holder. During characterization, the samples were rotated at a speed of 1 degree per second over a range of 180° while transmission X-ray microscopy (TXM) images of the samples were collected in the fly scan mode. TXM images were recorded by a 2k x 2k CCD camera using 2 x 2 pixel binning, providing a field of view of 40 x 40 x 40 µm³ and a pixel spatial resolution of 40 nm. 10 regions were scanned from the 4.5V and 4.8V samples, and 3 regions were scanned from the 4.6V sample. 3-dimensional tomographic images of the characterized sample regions were reconstructed from the acquired projection radiographs using the Python library PyXAS ⁴⁰.

5.4. Analysis of x-ray nanotomography images

Reconstructed tomographic images were imported into the visualization software Avizo 2019 ³⁹ as 3D voxel data and went through a semi-automatic, repeatable image processing procedure (Suppl. Fig. 9). The 3D images were first subject to grayscale normalization (0-255 intensity, 98th percentile) to ensure consistency in the contrast between particles, cracks, and background across different datasets. A bilateral filter is then applied to reduce noise. The filter radius was set to 3 pixels to balance the noise reduction and the retention of small features, and an intensity threshold of 50 was chosen so that it was larger than the variance of pixel brightness within the particles but smaller than the intensity difference between the particles and the background. After bilateral filtering, a "blurred" version of the images were obtained by applying a Gaussian blur filter with a radius of 5 pixels to smear the cracks within the particles and smooth the particle edges against the background.

Subsequently, the image processing splits into the particle and crack segmentation tasks. The two tasks generate separate datasets of binarized particle and crack images. Binarized particle images were obtained by selecting and segmenting individual particles using histogram thresholding and the manual segmentation editor (Magic Wand) in Avizo. When necessary, a 3D watershedding algorithm was performed to separate conjoined particles. Each particle was given a unique identifier and its surface area and volume were calculated in Avizo.

For the crack image dataset, voxels that belong to cracks were identified by performing the difference operation between the images before and after the application of the Gaussian blur filter, which were then binarized by histogram thresholding with an intensity threshold of 20 - 30. The obtained binary images highlight both cracks and particle edges. To remove particle edges from the crack images, the binarized particle images were 3D eroded by 3 pixels, which were applied to the crack images as a mask to set the values of the edge voxels to zero. 3D size filtering was

then performed to remove features smaller than 200 voxels, and 3D morphological closing with a radius of 3 pixels was used to fill the "holes" in the planar cracks that were not detected due to intensity variation in the original images. Finally, the binarized crack image dataset was manually inspected to remove false positives. Each individual crack was linked to the particle it belongs to in the binary particle image dataset, and its surface area and volume were also calculated.

5.5. Calculation of strain energy release rate

To illustrate the effect of particle size on the energy release caused by cracking propagation, we consider a prismatic particle of a given length (*L*) in 2D under plane strain conditions, with a surface-nucleated crack of size *a* in the middle of the particle (Suppl. Fig. 8a). Crack opening stress is generated by a phase transition with lattice mismatch $\varepsilon_a = 0.25\%$ and $\varepsilon_c = 3\%$ between phase I and II, which is comparable to that of the O3 \rightarrow H1-3 transition in LCO ³⁸. The strain energy release rate *G* is calculated for different *L/a* ratios in COMSOL by using the J integral method. The isotropic Young's modulus and Poisson ratio of LiCoO₂ (E = 174 GPa, v = 0.3) ⁴¹ are used in the calculation.

Acknowledgments

AH and MT were supported by the Department of Energy, Basic Energy Sciences under project DE-SC0019111. FW and ZL were supported by the National Science Foundation under project CMMI-1929949. YZ and YS acknowledges support from Shell International Exploration and Production Inc. Nanotomography experiments were performed at beamline 18-ID, National Synchrotron Light Source II, Brookhaven National Laboratory, which are supported by the U.S. DOE, Office of Science, Office of Basic Energy Sciences under Contract No. DE-AC02-

98CH10886. The authors acknowledge the Texas Advanced Computing Center (TACC) at The University of Texas at Austin for providing high-performance computing resources that have contributed to the research results.

References

- 1. W. H. Woodford, W. C. Carter, Y.-M. Chiang. Design Criteria for Electrochemical Shock Resistant Battery Electrodes. *Energy & Environmental Science* **5**, 8014 (2012).
- 2. G. W. Nam, N. Y. Park, K. J. Park, J. Yang, J. Liu, C. S. Yoon, Y. K. Sun. Capacity Fading of Ni-Rich NCA Cathodes: Effect of Microcracking Extent. *ACS Energy Letters* 4, 2995 (2019).
- 3. P. C. Tsai, B. H. Wen, M. Wolfman, M. J. Choe, M. S. Pan, L. Su, K. Thornton, J. Cabana, Y. M. Chiang. Single-particle Measurements of Electrochemical Kinetics in NMC and NCA cathodes for Li-ion Batteries. *Energy & Environmental Science* 11, 860 (2018).
- 4. H. Liu, M. Wolf, K. Karki, Y. S. Yu, E. A. Stach, J. Cabana, K. W. Chapman, P. J. Chupas. Intergranular Cracking as a Major Cause of Long-Term Capacity Fading of Layered Cathodes. *Nano Letters* 17, 3452 (2017).
- 5. B. Xu, C. R. Fell, M. F. Chi, Y. S. Meng. Identifying Surface Structural Changes in Layered Li-Excess Nickel Manganese Oxides in High Voltage Lithium Ion Batteries: A Joint Experimental and Theoretical Study. *Energy & Environmental Science* **4**, 2223 (2011).
- 6. F. Lin, D. Nordlund, Y. Y. Li, M. K. Quan, L. Cheng, T. C. Weng, Y. J. Liu, H. L. Xin, M. M. Doeff. Metal Segregation in Hierarchically Structured Cathode Materials for High-Energy Lithium Batteries. *Nature Energy* 1, 155004 (2016).
- 7. Z. H. Chen, Z. H. Lu, J. R. Dahn. Staging Phase Transitions in Li_xCoO₂. *Journal of The Electrochemical Society* **149**, A1604 (2002).
- 8. G. G. Amatucci, J. M. Tarascon, L. C. Klein. Cobalt Dissolution in LiCoO₂-based Non-Aqueous Rechargeable Batteries. *Solid State Ionics* **83**, 167 (1996).
- 9. Y. J. Kim, H. Kim, B. Kim, D. Ahn, J. G. Lee, T. J. Kim, D. Son, J. Cho, Y. W. Kim, B. Park. Electrochemical Stability of Thin-Film LiCoO₂ Cathodes by Aluminum-Oxide Coating. *Chemistry of Materials* **15**, 1505 (2003).
- L. Q. Mu, R. L. Lin, R. Xu, L. L. Han, S. H. Xia, D. Sokaras, J. D. Steiner, T. C. Weng, D. Nordlund, M. M. Doeff, Y. J. Liu, K. J. Zhao, H. L. L. Xin, F. Lin. Oxygen Release Induced Chemomechanical Breakdown of Layered Cathode Materials. *Nano Letters* 18, 3241 (2018).
- 11. Z. Zhu, D. W. Yu, Y. Yang, C. Su, Y. M. Huang, Y. H. Dong, I. Waluyo, B. M. Wang, A. Hunt, X. H. Yao, J. Lee, W. J. Xue, J. Li. Gradient Li-rich Oxide Cathode Particles Immunized Against Oxygen Release by a Molten Salt Treatment. *Nature Energy* **4**, 1049 (2019).
- 12. D. Aurbach, B. Markovsky, A. Rodkin, E. Levi, Y. S. Cohen, H. J. Kim, M. Schmidt. On the Capacity Fading of LiCoO₂ Intercalation Electrodes: the Effect of Cycling, Storage, Temperature, and Surface Film Forming Additives. *Electrochimica Acta* 47, 4291 (2002).
- 13. Z. H. Chen, J. R. Dahn. Methods to Obtain Excellent Capacity Retention in LiCoO₂ Cycled to 4.5 V. *Electrochimica Acta* **49**, 1079 (2004).
- J. E. Harlow, X. W. Ma, J. Li, E. Logan, Y. L. Liu, N. Zhang, L. Ma, S. L. Glazier, M. M. E. Cormier, M. Genovese, S. Buteau, A. Cameron, J. E. Stark, J. R. Dahn. A Wide Range of Testing Results on an Excellent Lithium-Ion Cell Chemistry to be used as Benchmarks for New Battery Technologies. *Journal of The Electrochemical Society* 166, A3031 (2019).

- 15. G. N. Qian, Y. T. Zhang, L. S. Li, R. X. Zhang, J. M. Xu, Z. J. Cheng, S. J. Xie, H. Wang, Q. L. Rao, Y. S. He, Y. B. Shen, L. W. Chen, M. Tang, Z. F. Ma. Single-Crystal Nickel-Rich Layered-Oxide Battery Cathode Materials: Synthesis, Electrochemistry, and Intra-granular Fracture. *Energy Storage Materials* 27, 140 (2020).
- 16. P. F. Yan, J. M. Zheng, M. Gu, J. Xiao, J. G. Zhang, C. M. Wang. Intragranular Cracking as a Critical Barrier for High-Voltage Usage of Layer-Structured Cathode for Lithium-Ion Batteries. *Nature Communications* **8**, 14101 (2017).
- 17. P. F. Yan, J. M. Zheng, T. W. Chen, L. L. Luo, Y. Y. Jiang, K. Wang, M. L. Sui, J. G. Zhang, S. L. Zhang, C. M. Wang. Coupling of Electrochemically Triggered Thermal and Mechanical Effects to Aggravate Failure in a Layered Cathode. *Nature Communications* 9, 2437 (2018).
- 18. Y. Y. Jiang, P. F. Yan, M. C. Yu, J. M. Li, H. Jiao, B. Zhou, M. L. Sui. Atomistic Mechanism of Cracking Degradation at Twin Boundary of LiCoO₂. *Nano Energy* **78**, 105364 (2020).
- 19. Q. Y. Lin, W. H. Guan, J. B. Zhou, J. Meng, W. Huang, T. Chen, Q. Gao, X. Wei, Y. W. Zeng, J. X. Li, Z. Zhang. Ni-Li Anti-Site Defect Induced Intragranular Cracking in Ni-Rich Layer-Structured Cathode. *Nano Energy* **76**, 105021 (2020).
- 20. J.-N. Zhang, Q. Li, C. Ouyang, X. Yu, M. Ge, X. Huang, E. Hu, C. Ma, S. Li, R. Xiao, W. Yang, Y. Chu, Y. Liu, H. Yu, X.-Q. Yang, X. Huang, L. Chen, H. Li. Trace Doping of Multiple Elements Enables Stable Battery Cycling of LiCoO₂ at 4.6 V. *Nature Energy* 4, 594 (2019).
- 21. Z. Zhu, D. W. Yu, Z. Shi, R. Gao, X. H. Xiao, I. Waluyo, M. Y. Ge, Y. H. Dong, W. J. Xue, G. Y. Xu, W. K. Lee, A. Hunt, J. Li. Gradient-Morph LiCoO₂ Single Crystals with Stabilized Energy Density above 3400 W h L⁻¹. *Energy & Environmental Science* 13, 1865 (2020).
- 22. H. F. Wang, Y. I. Jang, B. Y. Huang, D. R. Sadoway, Y. T. Chiang. TEM Study of Electrochemical Cycling-Induced Damage and Disorder in LiCoO₂ Cathodes for Rechargeable Lithium Batteries. *Journal of The Electrochemical Society* **146**, 473 (1999).
- 23. H. Kim, M. G. Kim, H. Y. Jeong, H. Nam, J. Cho. A New Coating Method for Alleviating Surface Degradation of LiNi_{0.6}Co_{0.2}Mn_{0.2}O₂ Cathode Material: Nanoscale Surface Treatment of Primary Particles. *Nano Letters* **15**, 2111 (2015).
- 24. Y. Xu, E. Hu, K. Zhang, X. Wang, V. Borzenets, Z. Sun, P. Pianetta, X. Yu, Y. Liu, X.-Q. Yang, H. Li. In situ Visualization of State-of-Charge Heterogeneity within a LiCoO₂ Particle that Evolves upon Cycling at Different Rates. *ACS Energy Letters* **2**, 1240 (2017).
- 25. Z. Liu, K. Han, Y. C. K. Chen-Wiegart, J. J. Wang, H. H. Kung, J. Wang, S. A. Barnett, K. T. Faber. X-ray Nanotomography Analysis of the Microstructural Evolution of LiMn₂O₄ Electrodes. *Journal of Power Sources* **360**, 460 (2017).
- 26. J. Wang, C. Eng, Y. C. Chen-Wiegart, J. Wang. Probing Three-Dimensional Sodiation-Desodiation Equilibrium in Sodium-Ion Batteries by In Situ Hard X-ray Nanotomography. *Nature Communications* **6**, 7496 (2015).
- F. Zhang, S. Lou, S. Li, Z. Yu, Q. Liu, A. Dai, C. Cao, M. F. Toney, M. Ge, X. Xiao, W. K. Lee, Y. Yao, J. Deng, T. Liu, Y. Tang, G. Yin, J. Lu, D. Su, J. Wang. Surface Regulation Enables High Stability of Single-Crystal Lithium-Ion Cathodes at High Voltage. *Nature Communications* 11, 3050 (2020).

- 28. S. Lou, Q. Liu, F. Zhang, Q. Liu, Z. Yu, T. Mu, Y. Zhao, J. Borovilas, Y. Chen, M. Ge, X. Xiao, W. K. Lee, G. Yin, Y. Yang, X. Sun, J. Wang. Insights into Interfacial Effect and Local Lithium-Ion Transport in Polycrystalline Cathodes of Solid-State Batteries.

 Nature Communications 11, 5700 (2020).
- 29. K. Teshima, S. Lee, Y. Mizuno, H. Inagaki, M. Hozumi, K. Kohama, K. Yubuta, T. Shishido, S. Oishi. Environmentally Friendly Growth of Well-Developed LiCoO₂ Crystals for Lithium-Ion Rechargeable Batteries Using a NaCl Flux. *Crystal Growth & Design* **10**, 4471 (2010).
- 30. D. Kramer, G. Ceder. Tailoring the Morphology of LiCoO₂: A First Principles Study. *Chemistry of Materials* **21**, 3799 (2009).
- 31. C. A. Marianetti, G. Kotliar, G. Ceder. A First-Order Mott Transition in Li_xCoO₂. *Nature Materials* **3**, 627 (2004).
- 32. J. N. Reimers, J. R. Dahn. Electrochemical and In Situ X-Ray-Diffraction Studies of Lithium Intercalation in Li_xCoO₂. *Journal of The Electrochemical Society* **139**, 2091 (1992).
- 33. A. Van der Ven, M. K. Aydinol, G. Ceder, G. Kresse, J. Hafner. First-Principles Investigation of Phase Stability in Li_xCoO₂. *Physical Review B* **58**, 2975 (1998).
- 34. A. Van der Ven, M. K. Aydinol, G. Ceder. First-Principles Evidence for Stage Ordering in Li_xCoO₂. *Journal of The Electrochemical Society* **145**, 2149 (1998).
- 35. H. Xia, L. Lu, Y. S. Meng, G. Ceder. Phase Transitions and High-Voltage Electrochemical Behavior of LiCoO₂ Thin Films Grown by Pulsed Laser Deposition. *Journal of The Electrochemical Society* **154**, A337 (2007).
- 36. Y. Bi, J. Tao, Y. Wu, L. Li, Y. Xu, E. Hu, B. Wu, J. Hu, C. Wang, J. G. Zhang, Y. Qi, J. Xiao. Reversible Planar Gliding and Microcracking in a Single-Crystalline Ni-Rich Cathode. *Science* **370**, 1313 (2020).
- 37. Y. Hu, X. Zhao, Z. Suo. Averting Cracks Caused by Insertion Reaction in Lithium–Ion Batteries. *Journal of Materials Research* **25**, 1007 (2011).
- 38. G. G. Amatucci, J. M. Tarascon, L. C. Klein. CoO₂, the End Member of the Li_xCoO₂ Solid Solution. *Journal of The Electrochemical Society* **143**, 1114 (1996).
- 39. S. Venkatraman, Y. Shin, A. Manthiram. Phase Relationships and Structural and Chemical Stabilities of Charged Li_{1-x}CoO₂-Delta and Li_{1-x}Ni_{0.85}Co_{0.15}O₂-Delta Cathodes. *Electrochemical and Solid State Letters* **6**, A9 (2003).
- 40. M. Y. Ge, W. K. Lee. PyXAS an Open-Source Package for 2D X-ray Near-Edge Spectroscopy Analysis. *Journal of Synchrotron Radiation* **27**, 567 (2020).
- 41. M. Qu, W. H. Woodford, J. M. Maloney, W. C. Carter, Y.-M. Chiang, K. J. Van Vliet. Nanomechanical Quantification of Elastic, Plastic, and Fracture Properties of LiCoO₂. *Advanced Energy Materials* **2**, 940 (2012).